Journal of Nuclear Medicine, published on February 22, 2019 as doi:10.2967/jnumed.118.220350

μPET/CT imaging of local and systemic immune response using ^{64}Cu-αCD11b

Qizhen Cao[1], Qian Huang[1], Chandra Mohan[2], Chun Li*[1]

[1]Department of Cancer Systems Imaging, The University of Texas MD Anderson Cancer Center, 1881 East Road, Houston, TX 77054, USA

[2]Department of Biomedical Engineering, University of Houston, 3605 Cullen Blvd, Houston, TX 77204-5060, USA

*Correspondence: Chun Li, PhD, Department of Cancer Systems Imaging, 1881 East Road–Unit 1907, The University of Texas MD Anderson Cancer Center, Houston, Texas 77054; Tel: 713-792-5182; Fax: 713-794-5456; E-mail: cli@mdanderson.org.

First author: Qizhen Cao, PhD, Department of Cancer Systems Imaging, 1881 East Road–Unit 1907, The University of Texas MD Anderson Cancer Center, Houston, Texas 77054; Tel: 713-792-3412; Fax: 713-794-5456; E-mail: qcao@mdanderson.org.

RUNNING TITLE: Monitor immune response with ^{64}Cu-αCD11b

FINANCIAL SUPPORT: This work was supported by the John S. Dunn Foundation and by National Institutes of Health/National Cancer Institute Cancer Center Support Grant P30CA016672.

ABSTRACT

Current noninvasive imaging methods for monitoring immune response were largely developed for interrogation of the local reaction. This study developed the radiotracer ^{64}Cu-labeled anti-CD11b (^{64}Cu-αCD11b) for longitudinal assessment of local and systemic immune response involving mobilization of CD11b^{+} myeloid cells by micro–positron emission tomography/computed tomography (μPET/CT). **Methods:** BALB/c mice with acute or chronic inflammation in the ears were induced by 12-o-tetradecanoylphorbol-13-acetate (TPA). Acute lung inflammation was induced by intratracheal lipopolysaccharides inoculation. αCD11b was conjugated with p-SCN-Bn-DOTA followed by labeling with ^{64}Cu. μPET/CT and biodistribution were evaluated at different times after intravenous injection of ^{64}Cu-αCD11b. Cell populations from bone marrows and spleens were analyzed by flow cytometry. **Results:** ^{64}Cu-αCD11b was primarily taken up by the bone marrow (BM) and spleen in normal mice. In comparison, ^{64}Cu-αCD11b uptake was significantly reduced in the BM and spleen of CD11b-knockout mice, indicating that ^{64}Cu-αCD11b selectively homed to CD11b^{+} myeloid cells *in vivo*. In mice with ear inflammation, for the local inflammatory response, ^{64}Cu-αCD11b μPET/CT revealed significantly higher ^{64}Cu-αCD11b uptake in the inflamed ears in the acute inflammation phase than the chronic phase, consistent with markedly increased infiltration of CD11b^{+} cells into the inflammatory lesions at the acute phase. Moreover, imaging of ^{64}Cu-αCD11b also showed the difference of mice systemic response for different inflammatory stage. Compared to uptake in normal mice, BM ^{64}Cu-αCD11b uptake in mice with ear inflammation was significantly lower in the acute phase and higher in the chronic phase, reflecting an initial mobilization of CD11b^{+} cells from the BM to the inflammatory foci followed by a compensatory regeneration of CD11b^{+} myeloid cells in the BM. Similarly, in mice with lung inflammation, ^{64}Cu-αCD11b μPET/CT

readily detected acute lung inflammation and recruitment of $CD11b^+$ myeloid cells from the BM. Immunohistochemistry staining and flow cytometry results confirmed the noninvasive imaging of PET/CT. **Conclusions:** ^{64}Cu-αCD11b μPET/CT successfully tracked ear and pulmonary inflammation in mice, and differentiated acute and chronic inflammation at local and systemic level. ^{64}Cu-αCD11b μPET/CT is a robust quantitative method for imaging of local and systemic immune responses.

Key Words: CD11b, PET/CT, Inflammation, Myeloid Cells, Systemic Immune Response

INTRODUCTION

When local inflammation develops, myeloid cells expand in the bone marrow (BM), enter the blood circulation, and travel to the inflamed sites. Some myeloid cells transit through secondary lymphoid organs (i.e., the spleen). Local diseases can also elicit a systemic immune response secondary to release of cytokines and chemokines from the disease sites. Yet other diseases are marked by systemic inflammation to begin with, as in the case of systemic autoimmune diseases. Because different types of tissue injury at different stages of disease progression elicit different local and systemic inflammatory responses, the ability to longitudinally interrogate the depletion, migration, and expansion of immune cells throughout the whole body will greatly facilitate disease characterization and guide selection of appropriate treatment regiments.

A number of imaging techniques have been used to monitor immune responses, including intravital optical imaging, magnetic resonance imaging (MRI), and nuclear imaging, but all of these techniques have limitations (*1,2*). Intravital optical imaging can directly visualize the dynamics of interactions among different types of cells, however this technique suffers from limited penetration depth (*3*). MRI is useful for monitoring trafficking of infused immune cells labeled *ex vivo*, but is not yet suitable for imaging biomarkers in specific immune cell populations labeled *in vivo*. In the area of nuclear imaging, several radiotracers have been reported to permit monitoring of inflammation on the basis of changes in metabolism (*4-6*) or *ex vivo* labeling of inflammatory cells or inflammatory cytokines (*7,8*), but it is limited by labeling efficiency and the labor-intensive cell labeling procedures (*9*). To date, few studies reported visualization of both the local and the systemic immune responses to inflammatory and neoplastic diseases (*10*).

Most innate inflammatory cells including granulocytes, monocytes, and macrophages express CD11b (also known as αM-integrin or Mac-1) on their cell surface (*11,12*). We hypothesized that CD11b could be used as an imageable biomarker for noninvasive assessment of local and systemic immune responses. In this work, we report the application of μPET/CT with ^{64}Cu-αCD11b in monitoring the mobilization of CD11b^{+} myeloid cells from the BM to secondary lymphoid organs and to local inflammatory lesions.

MATERIALS AND METHODS

Reagents

Rat anti-mouse CD11b antibody (αCD11b, clone M1/70, Catalog number 14-0112), rat anti-mouse CD11b phycoerythrin (clone M1/70), rat anti-mouse Gr-1 PerCP-Cyanine5.5 (clone RB6-8C5), and rat anti-mouse Ly6C allophycocyanin (clone HK1.4) were purchased from eBioscience Inc. (San Diego, CA). p-SCN-Bn-DOTA was purchased from Macrocyclics, Inc. (Dallas, TX). 12-*o*-Tetradecanoylphorbol-13-acetate (TPA) was purchased from Sigma-Aldrich (St. Louis, MO). Lipopolysaccharide (*Escherichia coli* 0111) was purchased from List Biologics (Campbell, CA). $^{64}CuCl_2$ and ^{18}F-fluorodeoxyglucose (^{18}F-FDG) were obtained from the Cyclotron Radiochemistry Facility of The University of Texas MD Anderson Cancer Center (Houston, TX).

DOTA Conjugation and Radiolabeling

p-SCN-Bn-DOTA was added to αCD11b or isotype-matched IgG at p-SCN-Bn-DOTA-to-antibody molar ratios of 50:1 in 0.1 mol/L sodium bicarbonate buffer (pH 8.5). The resulting DOTA-αCD11b conjugate was purified using PD-10 column, and the DOTA number for DOTA-αCD11b was measured (Supplemental Table 1). For radiolabeling, $^{64}CuCl_2$ was diluted with

sodium acetate buffer (pH 6.0), and the pH of the solution was adjusted to pH 6.0 with 1 N of NaOH. Each DOTA-antibody conjugate was then added into $^{64}CuCl_2$ solution (10 μg of DOTA-antibody per 37 MBq of ^{64}Cu) and incubated for 1 h at 38°C with constant shaking. ^{64}Cu-αCD11b or ^{64}Cu-IgG was purified by passage through a PD-10 column.

Animal Models

All animal experiments were performed in compliance with the guidelines for care and use of research animals established by the Institutional Animal Care and Use Committee of The University of Texas MD Anderson Cancer Center (IACUC Protocol #: 00001333). Female BALB/c mice and C57BL/6 mice (6-8 weeks of age) were obtained from Taconic (Cambridge City, IN). $CD11b^{-/-}$ (CD11b knockout) C57BL/6 mice (B6.129S4-Itgamtm1Myd/J, Stock number: 003991) were purchased from The Jackson Laboratory (Bar Harbor, ME).

Ear Inflammation Model: Twenty microliters of TPA solution (100 μg/mL in acetone) was topically applied to the ventral and dorsal sides of the right ear of BALB/c mice 1, 4, or 11 times (*8,13*).

Lung Inflammation Model: BALB/c mice were anesthetized with 2% isoflurane, and then 20 μg of lipopolysaccharide in 0.1 mL of saline was given intratracheally. Control animals were given 0.1 mL of saline intratracheally (*14*).

μPET/CT and Biodistribution

μPET/CT was performed using an Inveon scanner (Siemens Medical Solutions, Erlangen, Germany) or Albira scanner (Bruker, Billerica, MA) after intravenous injection of ^{64}Cu-αCD11b or its corresponding isotype antibody control ^{64}Cu-IgG at a dose of 3.7 MBq/mouse (1.22 ± 0.22 μg antibody/3.7 MBq/mouse). Mice were euthanized 24 h or 48 h after injection. Blood, major organs, and inflamed tissue specimens were collected, wet-weighed, and counted with a gamma

counter (Packard, Waltham, MA). The results were reported as mean %ID/g and standard deviation (n = 3/group).

Autoradiography

Immediately after the μPET/CT imaging, the ears were harvested and then taped to a chilled autoradiography cassette containing a Super Resolution screen (Packard, Meriden, CT) and stored overnight at 4°C. Screens were scanned with a Fujifilm FLA-5100 imaging system (Stamford, CT).

Hemoxylin-Eosin (H&E) and Immunohistochemistry (IHC) Staining

For H&E staining, organ samples were fixed in 10% (v/v) buffered formalin and embedded in paraffin. Five-micrometer-thick sections were cut and stained with H&E. For IHC staining, the formalin-fixed paraffin sections were deparaffinized, rehydrated, and incubated in 3% aqueous H_2O_2 to block the endogenous peroxidase activity. After blocking with 2% normal horse serum, the primary antibody rat anti-mouse Ly6G (eBioscience Inc, San Diego, CA) at 1:50 dilution were added and incubated at 4ºC overnight. IHC reaction was performed by using Vectastain ELITE ABC HRP kit (Rat IgG) (Vector Laboratories, Burlingame, CA).

Flow Cytometry

BM cells were obtained from mouse femur according to reported procedures (*15*). For flow cytometry, fluorescence probes were added to single cell suspensions prepared from samples obtained from BM or spleen, and cells were incubated on ice for 1 h. After washing with PBS 3 times, cells were examined on a FACSCalibur flow cytometer or LSRFortessa X-20 Analyzer (Becton Dickinson, Mountain View, CA), and analyzed with FlowJo software (Tree Star, Inc., Ashland, OR). The following antibodies were used: rat anti-mouse Ly6G-FITC, rat anti-mouse CD11b-phycoerythrin, rat anti-mouse Gr-1-PerCP-Cyanine5.5, and anti-mouse

Ly6C-allophycocyanin.

Statistics

Statistical significance was analyzed with IBM SPSS statistics 24 software using one-way ANOVA. P values < 0.05 were considered statistically significant.

RESULTS

^{64}Cu-αCD11b Selectively Binds to CD11b^{+} Myeloid Cells

The binding affinity between ^{64}Cu-αCD11b and mouse BM cells was determined by a competitive displacement assay. The 50% inhibitory concentration between ^{64}Cu-αCD11b and nonradioactive αCD11b was $1.56\times10^{-10} \pm 5.14\times10^{-11}$ mol/L (Supplemental Fig. 1).

Figure 1A compares μPET/CT images acquired at various times after intravenous injection of ^{64}Cu-αCD11b in normal (i.e., CD11b sufficient) and CD11b knockout (CD11b$^{-/-}$) C57BL/6 mice. In normal mice, the radiotracer was primarily distributed to the bone, spleen, and liver. Strong signals from the spinal cord, hip bones and joints could be visualized as early as 1 h after injection and peaked at 5 h after injection, suggesting robust uptake of ^{64}Cu-αCD11b to the BM (which bears CD11b^{+} cells). The high uptake of ^{64}Cu-αCD11b in the spleen is consistent with the fact that the mouse spleen harbors half of the body's monocytes within its red pulp (*16*). In contrast, in the CD11b knockout mice, the amount of ^{64}Cu-αCD11b in the blood pool (heart) was significantly higher than that in normal mice at all time point studies ($p<0.001$). While the uptake of ^{64}Cu-αCD11b in the BM and spleen was significantly lower in the CD11b knockout mice than in the wildtype mice (Fig. 1A, Supplemental Figs. 2 and 3). Uptake of ^{64}Cu-αCD11b in the liver was also greater in knockout mice, likely in part because of increased blood pool

activity. The observation that uptake in the heart and liver is non-specific is also supported by the use of non-specific IgG, as discussed below.

Flow cytometry analysis performed 48 h after radiotracer injection confirmed that the percentage of $CD11b^+$ cells in the BM was 26.3 ± 3.0% in normal mice versus 0.27 ± 0.01% in $CD11b^{-/-}$ mice (Fig. 1B, Supplemental Fig. 4). Likewise, the percentage of $CD11b^+$ cells in the spleen was 2.9 ± 0.3% in normal mice versus 0.02 ± 0.01% in $CD11b^{-/-}$ mice (Fig. 1B). These data indicate that ^{64}Cu-αCD11b specifically bound to $CD11b^+$ myeloid cells *in vivo*.

After peaking at 5 h, the uptake of ^{64}Cu-αCD11b in the BM of normal mice steadily and significantly decreased from 5 h to 24 h and 48 h after injection ($p<0.001$), while uptake of ^{64}Cu-αCD11b in the BM of knockout mice remained low at background levels, unchanged from 24 to 48 h (Supplemental Figs. 3C and 3D). This might be attributed to either redistribution of ^{64}Cu-αCD11b-bound myeloid cells from the BM to the peripheral circulation in normal mice, clearance of radiotracer, or both.

In normal BALB/C mice, ^{64}Cu-αCD11b displayed a distribution pattern similar to that in normal C57BL/6 mice: BM, spleen, and liver were the organs with major radiotracer uptake (Supplemental Figs. 5A and 5B). $CD11b^+$ cells were the major cell population in the BM of BALB/c mice: 37.5 ± 1.92% of the BM cells expressed CD11b (Supplemental Fig. 5C).

^{64}Cu-αCD11b µPET Differentiates Different Stages of TPA-induced Local Inflammation

We first investigated changes in the distribution pattern of $CD11b^+$ myeloid cells at the local level in response to TPA-induced inflammation in the ears of BALB/c mice. µPET/CT images acquired 24 h after intravenous injection of ^{64}Cu-αCD11b showed significantly higher uptake in the inflamed ears 30 h after a single TPA challenge, during the acute inflammation

stage (Fig. 2A). In comparison, when 4 or 11 TPA challenges were administered and imaging was done 8 or 22 days after the first challenge during the chronic inflammation stage, significantly less $CD11b^+$ signal was seen within the inflamed ear. There was minimal radiotracer uptake in the contralateral, unchallenged ears or ears of normal mice (Fig. 2A). These μPET/CT data were confirmed by classical biodistribution study (Fig. 2B).

To exclude the possibility of nonspecific uptake of antibody in acute inflammation, we used ^{64}Cu-IgG as a control. μPET/CT showed low deposition of ^{64}Cu-IgG in the bone and spleen (Fig. 2C), with most of the signal being detected in the heart and liver, a distribution pattern typical of nonspecific antibodies (*17*). Quantitative analysis showed that ^{64}Cu-αCD11b uptake in the ears with acute inflammation was 3.8 times that of ^{64}Cu-IgG ($p < 0.001$) further supporting that ^{64}Cu-αCD11b selectively bound to $CD11b^+$ myeloid cells in acute inflammatory lesions *in vivo*.IHC staining of Ly6G, a marker for myeloid-derived granulocytes and neutrophils ($CD11b^+Ly6G^+$) (*18*), showed infiltration of the inflamed ears by a large number of $Ly6G^+$ neutrophils 30 h after a single TPA challenge (Fig. 3A). Neutrophils are among the first inflammatory cells to migrate towards a site of inflammation. In contrast, multiple applications of TPA produced a chronic inflammatory reaction characterized by increased ear thickness (Supplemental Fig. 6) and diminished $Ly6G^+$ neutrophils (Fig. 3A).

Autoradiography 24 h after intravenous injection of ^{64}Cu-αCD11b showed minimal radioactivity in normal ears (Fig. 3B), and intense radioactivity in ears following a single TPA challenge, consistent with extensive neutrophil infiltration, but decreased radioactivity in ears with 4 or 11 TPA challenges, consistent with decreased neutrophil infiltration in ears with chronic inflammation.

μPET with ^{18}F-FDG, which tracks elevated glucose metabolism, is a clinically

established technique to assess metabolic activity of inflammatory process. In both acute and chronic inflammation in BALB/c mice, the inflamed ears were barely visible with ^{18}F-FDG µPET/CT (Fig. 3C, Supplemental Fig. 7). Nevertheless, the uptake of ^{18}F-FDG in the ears after a single TPA challenge and after 8 TPA challenges were significantly higher than the uptake in normal ears , indicating low but increased metabolic activity in the inflamed ears. On comparison, the uptake of ^{18}F-FDG in the inflamed ears (0.45-1.00 %ID/g) were much lower than the uptakes of ^{64}Cu-αCD11b in the ears with either acute inflammation (38.7 %ID/g) or chronic inflammation (3.6-6.9 %ID/g). Taken together, these data indicate that ^{64}Cu-αCD11b µPET/CT is more effective in differentiating acute and chronic inflammation compared to tracking changes in metabolic activity with ^{18}F-FDG µPET/CT.

µPET with ^{64}Cu-αCD11b Detects TPA-induced Inflammation at Systemic Level

In mice with ear inflammation, ^{64}Cu-αCD11b µPET/CT revealed a small decrease in the uptake of ^{64}Cu-αCD11b in the BM after a single TPA challenge. Interestingly, BM uptake of ^{64}Cu-αCD11b was significantly higher after 4 and 11 TPA challenges, compared to a single TPA injection (Fig. 2A). ^{64}Cu-αCD11b uptake in the spleen increased after a single TPA challenge and further increased following additional TPA challenges (Fig. 2A; Supplemental Fig. 8). Uptakes of radiotracer in the bone (including BM) of normal mice and mice with 1, 4, and 11 TPA challenges were 13.1± 0.25, 10.6 ± 1.34, 15.9 ± 1.55, and 16.3 ± 0.69 %ID/g ($p < 0.05$ for all comparisons with normal mice), respectively (Fig. 2B). These data likely underestimated the uptake values in the BM because the weight of the cortical bone was included in the calculation of ID%/g values. Thus, changes of CD11b$^+$ myeloid cells in the BM and spleen could be readily visualized using ^{64}Cu-αCD11b µPET/CT.

Flow cytometry analysis showed that $CD11b^+$ cells in the BM cells of normal mice and mice with 1, 4, and 11 TPA challenges were 36.5 ± 4.8%, 28.5 ± 4.4%, 61.2 ± 8.8%, and 53.2 ± 7.5%, respectively (Fig. 4A, 4B). Furthermore, the $CD11b^+Gr\text{-}1^+$ double-positive cells, consisting of myeloid progenitors and immature granulocytes, macrophages, and dendritic cells, in the BM cells of normal mice and mice with 1, 4, and 11 TPA challenges were 32.3 ± 2.0%, 23.9 ± 2.7%, 55.5 ± 4.1%, and 47.9 ± 4.7%, respectively (Fig. 4A, 4B). These findings were consistent with the ^{64}Cu-αCD11b μPET/CT data that revealed an initial depletion of $CD11b^+$ cells in acute inflammation followed by an expansion of $CD11b^+$ cells in chronic inflammation in the BM (Fig. 2A).

μPET with ^{64}Cu-αCD11b Detects Endotoxin-induced Lung Inflammation at Local and Systemic Levels

Lung inflammation induced by intratracheal lipopolysaccharide closely reflects human lung inflammation (*19*). μPET/CT 24 h after intravenous injection of ^{64}Cu-αCD11b (28 h after intra-tracheal injection of lipopolysaccharide) revealed higher radiotracer accumulation in the lungs, spleen, and liver and lower radiotracer signal in the BM of mice with lipopolysaccharide treatment (Fig. 5A). The lipopolysaccharide-treated lungs showed increased thickness of alveolar walls and increased neutrophil infiltration (Fig. 5B). There was significantly higher uptake of ^{64}Cu-αCD11b in the lungs of lipopolysaccharide-treated mice (6.23 ± 1.57 %ID/cc) than in the lungs of control mice (2.03 ± 0.09, $p < 0.01$), 24 h after radiotracer injection (Fig. 5C). Lipopolysaccharide-treated mice exhibited significantly lower radiotracer uptake in the spine compared to control normal mice (8.8 ± 1.2 %ID/cc vs 12.9 ± 1.2, $p < 0.05$) and femoral BM (7.4 ± 0.7 %ID/cc vs 13.8 ± 2.1, $p < 0.01$). These lipopolysaccharide-treated mice also showed

significantly higher radiotracer uptake in the spleen (24.3 ± 0.4 %ID/cc vs 16.4 ± 1.5; $p < 0.001$), as well as the liver (19.2 ± 0.7 %ID/cc vs 10.4 ± 0.7; $p < 0.001$). These $CD11b^+$ cellular distribution patterns were similar to those observed in mice with TPA-induced acute ear inflammation.

Flow cytometry data revealed that the population of $CD11b^+$ cells in the BM of lipopolysaccharide-treated mice decreased significantly compared to that of the control mice (Fig. 5D; Supplemental Fig. 9A), consistent with the ^{64}Cu-αCD11b μPET imaging data. $CD11b^+Gr\text{-}1^+$ cells consist of 2 major subsets: $Ly6G^+Ly6C^{low}$ granulocytic cells and $Ly6G^-Ly6C^+$ monocytic cells. Results showed a significant decrease in $Ly6G^+Ly6C^{low}$ granulocytic cells but not $Ly6G^-Ly6C^+$ monocytic cells in the BM of lipopolysaccharide-treated mice compared to values in control mice (Fig. 5D; Supplemental Fig. 9B). These results also demonstrated that ^{64}Cu-αCD11b μPET/CT permitted visualization of the dynamic innate immune response at both the local inflammation site and at the whole-body level, following a localized immune challenge.

DISCUSSION

In this study, we found that ^{64}Cu-αCD11b specifically and robustly labeled $CD11b^+$ myeloid cells *in vitro* and *in vivo*. ^{64}Cu-αCD11b μPET/CT could track and quantify changes in the number of $CD11b^+$ cells both at the local level at the inflammatory sites and at the systemic level in the BM and the secondary lymphoid organ (spleen).

Several lines of evidence suggest that ^{64}Cu-αCD11b specifically bound to $CD11b^+$ cells *in vivo*. First, whereas the CD11b-sufficient C57BL/6 mice exhibited high radiotracer uptake in

the BM and spleen, reservoir organs for $CD11b^+$ cells, the CD11b-knockout mice had significantly lower uptake of the radiotracer in these organs and a significantly higher amount of ^{64}Cu-αCD11b in the blood pool (particularly the heart). Second, deposition of nonspecific ^{64}Cu-IgG in the BM and spleen of ear inflammation mice was significantly lower than the deposition of ^{64}Cu-αCD11b in these organs.

Our study shows that ^{64}Cu-αCD11b μPET/CT could be used to differentiate acute and chronic local inflammation. ^{64}Cu-αCD11b μPET/CT clearly delineated inflamed ears in the acute inflammation phase, and reduced radiotracer uptake in the chronic inflammation phase. IHC staining confirmed the presence of a large number of neutrophil granulocytes ($CD11b^+Ly6G^+$) within the inflammatory lesions in the acute phase but only a small number of $CD11b^+Ly6G^+$ granulocytes infiltrating the lesions in the chronic phase. It is known that during chronic inflammation, other types of immune cells responsible for tissue repair and remodeling, such as lymphocytes and fibroblasts that do not express CD11b, are the dominant inflammatory cells (*20*).

Importantly, our studies suggest that ^{64}Cu-αCD11b μPET/CT may be used to noninvasively interrogate mobilization of innate immune cells from the BM through the spleen/liver compartments to the diseased sites. In mice inflammation models, ^{64}Cu-αCD11b μPET/CT demonstrated a decrease in BM radiotracer uptake in the acute inflammation phase and a significant increase in BM radiotracer uptake in the chronic inflammation phases. These imaging data were consistent with reduced $CD11b^+$ and $CD11b^+Ly6G^+$ cells in the BM in the acute inflammation phase and increased $CD11b^+$ and $CD11b^+Ly6G^+$ cells in the BM during chronic inflammation. Myeloid cells, in particular neutrophils, provide an important early defense mechanism against acute infection and inflammation. Under normal circumstances, most

of the neutrophil pool is stored in the BM; only a small fraction of neutrophils enter the blood circulation at any given time (<2% of 65 million in the mouse) (*21*). Thus, the immediate need for a large number of neutrophils in the case of acute inflammation cannot be met by circulating neutrophils in the blood pool, leading to rapid mobilization of neutrophils from the BM. This dynamic but transient process of recruiting $CD11b^+$ myeloid cells and $CD11b^+Ly6G^+$ granulocytes from the BM and their trapping in the spleen and liver were readily detected and quantified using ^{64}Cu-αCD11b μPET/CT. In the chronic inflammation phase, the system may be signaled to produce more myeloid cells, though this needs verification using BrdU labeling studies. Likewise, extramedullary myelopoietic activity in the spleen may have contributed to the increased uptake of ^{64}Cu-αCD11b in the spleen, though this hypothesis needs further verification. To sum, ^{64}Cu-αCD11b μPET/CT represents a powerful tool for studying the dynamics of the innate immune response locally and systemically in living animals.

Our finding that $CD11b^+$ myeloid cells in the BM were readily accessible to ^{64}Cu-αCD11b contrasts with the findings reported by Rashidian et al. (*22*) who used a much smaller variable domain of a camelid heavy-chain-only antibody targeting CD11b (~15 kDa), ^{18}F-VHHDC13. Although this ^{18}F-labeled probe showed uptake in spleen and lymph nodes, there was no uptake in the BM. It may be that the αCD11b used in our study and the camelid antibody VHHDC13 bind to different CD11b epitopes, which may be differentially expressed in BM-derived myeloid cells and in tumor-associated myeloid cells. It is also possible that the much larger αCD11b (~150 kDa) has a longer blood half-life than that of VHH antibody (~20 min) and thus a greater likelihood of delivery to the cells in the BM.

Our study has a few limitations. First, CD11b is expressed on several different types of myeloid cells, and on a few non-myeloid cells as well. Additional imaging markers are needed in

order to enhance cellular resolution. Second, the system-wide myeloid cell trafficking studies need to be expanded with accurate enumeration of CD11b cell numbers in various primary and secondary immune compartments, fortified with BrdU labeling studies. Third, while we have established that ^{64}Cu-αCD11b could image CD11b in murine models of disease, clinical significance of this approach in comparison to other imaging methods currently utilized to assess inflammation remains to be determined.

In conclusion, μPET/CT imaging with ^{64}Cu-αCD11b has the potential for tracking and quantifying changes in CD11b^{+} cell numbers longitudinally and non-invasively both locally as well as systemically.

AUTHOR CONTRIBUTIONS

Dr. Qizhen Cao designed and performed experiments, analyzed data, and wrote the manuscript; Qian Huang performed some experiments; Dr. Chandra Mohan analyzed and interpreted data; Dr. Chun Li designed experiments, analyzed data, and wrote the paper.

ACKNOWLEDGMENTS

We thank Stephanie Deming for editing this manuscript and Daniel Young for help with preparation of samples for histologic examinations. We thank the support from the Flow Cytometry & Cellular Imaging Core Facility and Small Animal Imaging Facility at MD Anderson Cancer Center.

CONFLICT OF INTEREST STATEMENT

The authors have declared that no conflict of interest exists.

REFERENCES

1. Hildebrandt IJ, Gambhir SS. Molecular imaging applications for immunology. *Clin Immunol*. 2004;111:210-224.
2. Gross S, Moss BL, Piwnica-Worms D. Veni, vidi, vici: in vivo molecular imaging of immune response. *Immunity*. 2007;27:533-538.
3. Germain RN, Miller MJ, Dustin ML, Nussenzweig MC. Dynamic imaging of the immune system: progress, pitfalls and promise. *Nat Rev Immunol*. 2006;6:497-507.
4. Laitinen IE, Luoto P, Nagren K, et al. Uptake of 11C-choline in mouse atherosclerotic plaques. *J Nucl Med*. 2010;51:798-802.
5. Rudd JH, Myers KS, Bansilal S, et al. Atherosclerosis inflammation imaging with 18F-FDG PET: carotid, iliac, and femoral uptake reproducibility, quantification methods, and recommendations. *J Nucl Med*. 2008;49:871-878.
6. Glaudemans AW, de Vries EF, Galli F, Dierckx RA, Slart RH, Signore A. The use of (18)F-FDG-PET/CT for diagnosis and treatment monitoring of inflammatory and infectious diseases. *Clin Dev Immunol*. 2013;2013:623036.
7. Peters AM, Saverymuttu SH, Reavy HJ, Danpure HJ, Osman S, Lavender JP. Imaging of inflammation with indium-111 tropolonate labeled leukocytes. *J Nucl Med*. 1983;24:39-44.
8. Cao Q, Cai W, Li ZB, et al. PET imaging of acute and chronic inflammation in living mice. *Eur J Nucl Med Mol Imaging*. 2007;34:1832-1842.
9. Palestro CJ. Radionuclide imaging of musculoskeletal infection: A Review. *J Nucl Med*. 2016;57:1406-1412.
10. Hammoud DA. Molecular imaging of inflammation: current status. *J Nucl Med*. 2016;57:1161-1165.

11. Gordon S, Taylor PR. Monocyte and macrophage heterogeneity. *Nat Rev Immunol*. 2005;5:953-964.
12. Gabrilovich DI, Nagaraj S. Myeloid-derived suppressor cells as regulators of the immune system. *Nat Rev Immunol*. 2009;9:162-174.
13. Murakawa M, Yamaoka K, Tanaka Y, Fukuda Y. Involvement of tumor necrosis factor (TNF)-alpha in phorbol ester 12-O-tetradecanoylphorbol-13-acetate (TPA)-induced skin edema in mice. *Biochem Pharmacol*. 2006;71:1331-1336.
14. Li XC, Miyasaka M, Issekutz TB. Blood monocyte migration to acute lung inflammation involves both CD11/CD18 and very late activation antigen-4-dependent and independent pathways. *J Immunol*. 1998;161:6258-6264.
15. Weischenfeldt J, Porse B. Bone marrow-derived macrophages (BMM): isolation and applications. *CSH Protoc*. 2008;2008:pdb prot5080.
16. Swirski FK, Nahrendorf M, Etzrodt M, et al. Identification of splenic reservoir monocytes and their deployment to inflammatory sites. *Science*. 2009;325:612-616.
17. Wipke BT, Wang Z, Kim J, McCarthy TJ, Allen PM. Dynamic visualization of a joint-specific autoimmune response through positron emission tomography. *Nat Immunol*. 2002;3:366-372.
18. Kolaczkowska E, Kubes P. Neutrophil recruitment and function in health and inflammation. *Nat Rev Immunol*. 2013;13:159-175.
19. Rittirsch D, Flierl MA, Day DE, et al. Acute lung injury induced by lipopolysaccharide is independent of complement activation. *J Immunol*. 2008;180:7664-7672.

20. Aldaz CM, Conti CJ, Gimenez IB, Slaga TJ, Klein-Szanto AJ. Cutaneous changes during prolonged application of 12-O-tetradecanoylphorbol-13-acetate on mouse skin and residual effects after cessation of treatment. *Cancer Res*. 1985;45:2753-2759.

21. Raffaghello L, Bianchi G, Bertolotto M, et al. Human mesenchymal stem cells inhibit neutrophil apoptosis: a model for neutrophil preservation in the bone marrow niche. *Stem Cells*. 2008;26:151-162.

22. Rashidian M, Keliher EJ, Bilate AM, et al. Noninvasive imaging of immune responses. *Proc Natl Acad Sci U S A*. 2015;112:6146-6151.

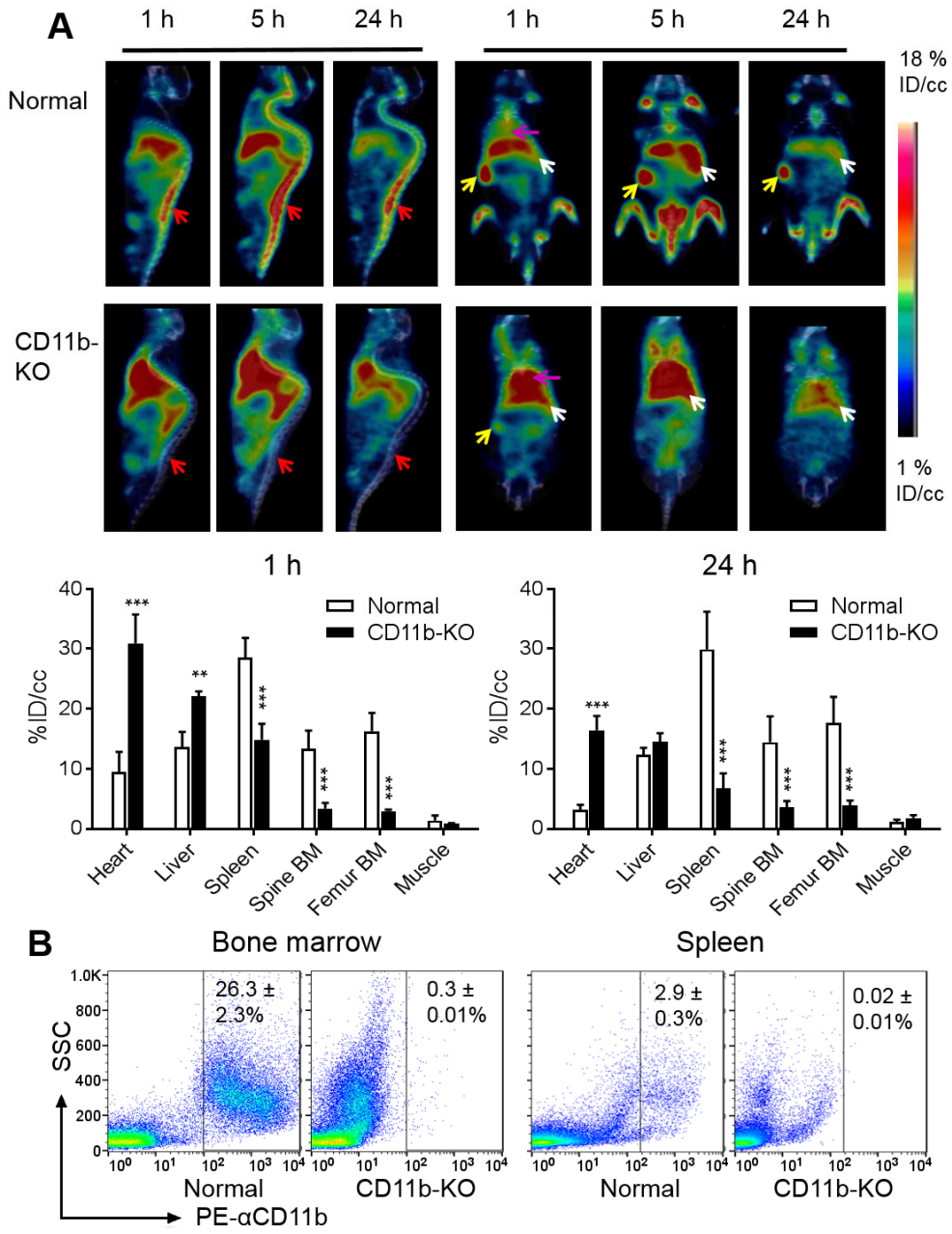

Figure 1. ^{64}Cu-αCD11b µPET/CT in normal (CD11b-sufficient) and CD11b-knockout C57BL/6 mice. (**A**) Representative µPET/CT images of normal mice (top) and CD11b-knockout (KO) mice (bottom). Red arrows: bone marrow; yellow arrows: spleen; white arrows: liver; purple arrows: heart. PET quantification of ^{64}Cu-αCD11b uptake in major organs at 1 h and 24 h after intravenous injection of the radiotracer. BM, bone marrow. (**B**) Flow cytometry analysis of CD11b^{+} cells in the bone marrow and spleen of normal and CD11b knockout (CD11b-KO) mice. All data are expressed as mean ± SD (n=3/group). **p<0.01; ***p<0.001.

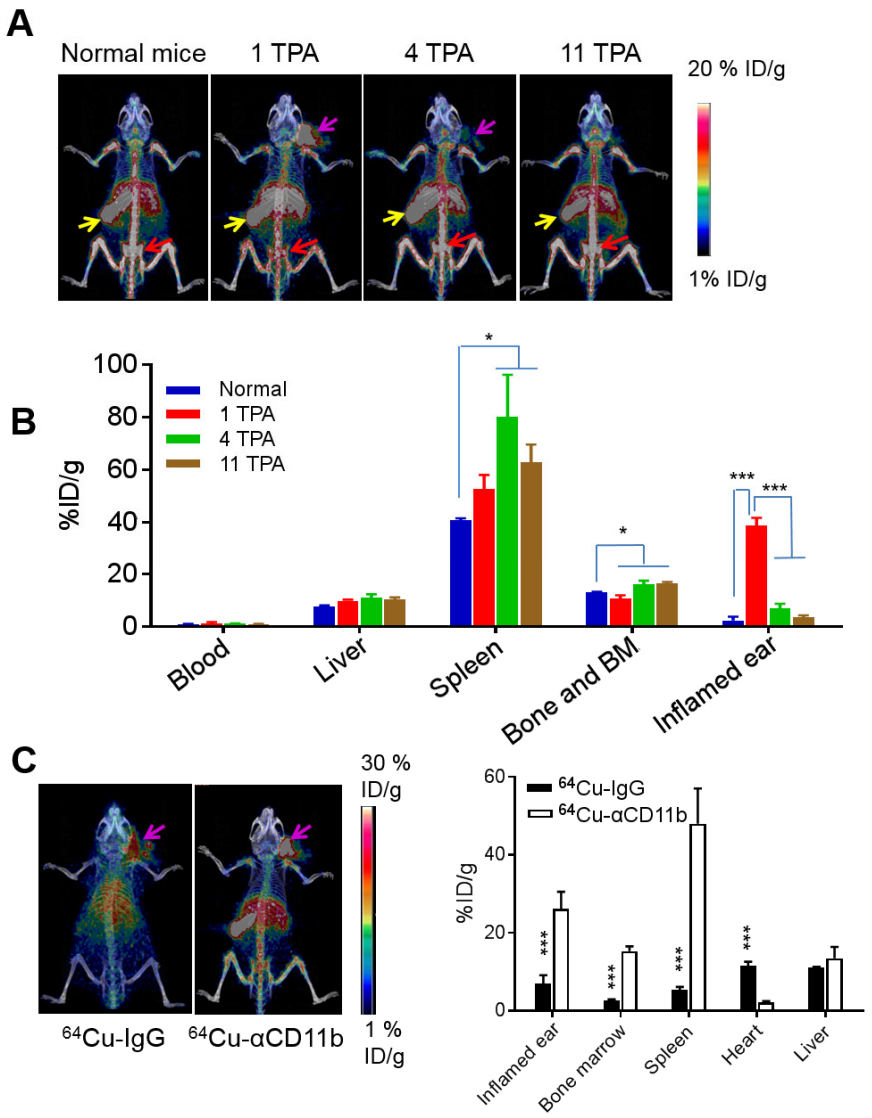

Figure 2. ^{64}Cu-αCD11b µPET/CT and biodistribution of ^{64}Cu-αCD11b in BALB/c mice with TPA-induced acute and chronic ear inflammation. (**A**) Representative µPET/CT images of a normal mouse; a mouse with acute inflammatory focus after a single TPA challenge in the ear; and mice with chronic inflammatory foci after 4 and 11 TPA challenges. Images were acquired 24 h after intravenous injection of ^{64}Cu-αCD11b. Purple arrows: inflamed ears; red arrows: bone marrow; yellow arrows: spleen. (**B**) Biodistribution of ^{64}Cu-αCD11b in normal mice; mice with 1, 4, and 11 TPA challenges. Data were collected 48 h after intravenous injection of ^{64}Cu-αCD11b. (**C**) Representative µPET/CT images and corresponding quantitative analysis comparing ^{64}Cu-IgG control antibody to ^{64}Cu-αCD11b in mice with acute ear inflammation after a single TPA challenge. Data are expressed as mean ± SD (n=3/group). *p<0.05; ***p<0.001.

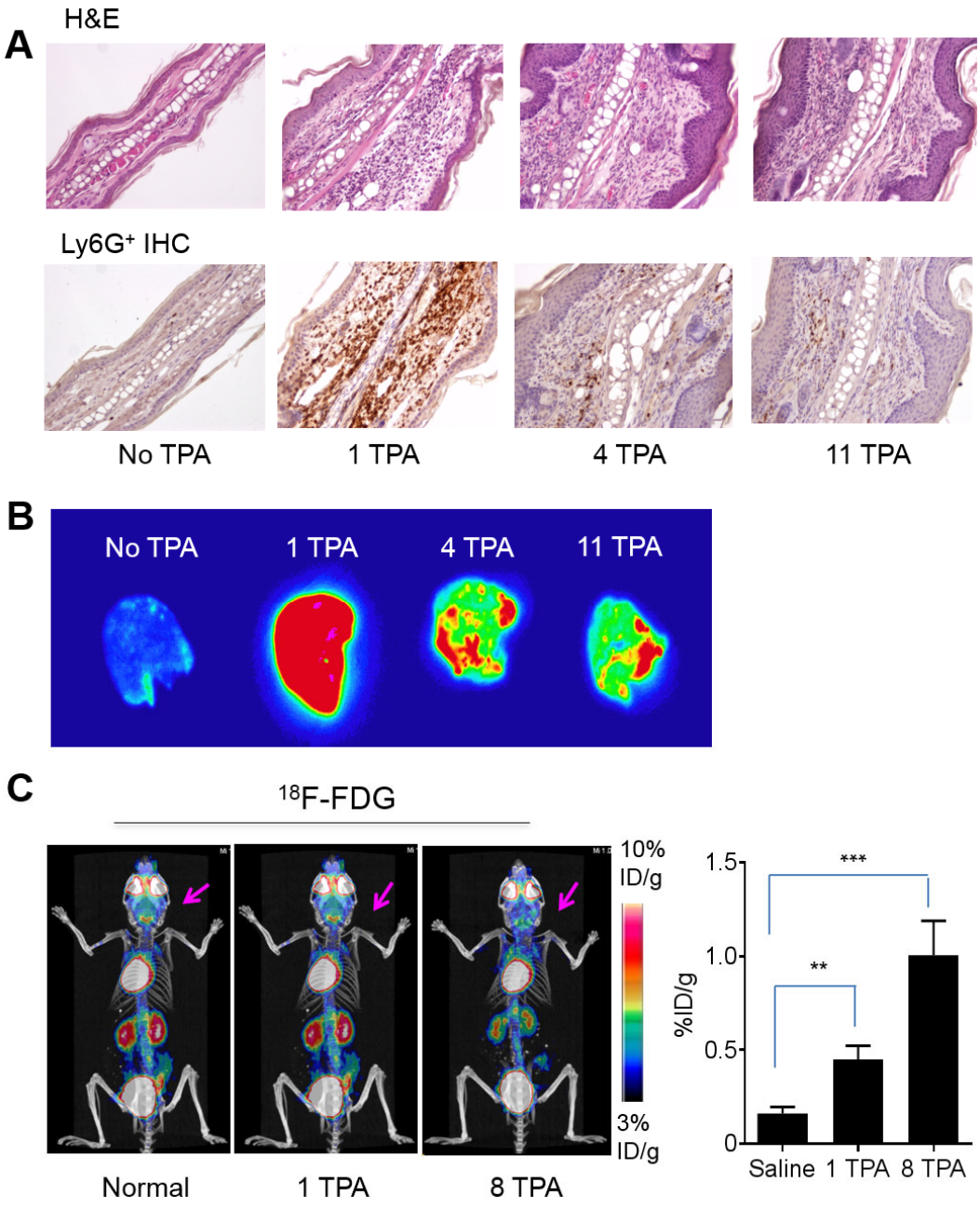

Figure 3. Histologic and IHC confirmation of local inflammatory response in TPA-treated ears. (**A**) Representative images of sections of H&E-stained and IHC-stained inflamed ears (200×). (**B**) Autoradiographs of ears from mice with different TPA treatments removed 48 h after intravenous injection of ^{64}Cu-αCD11b. (**C**) Representative ^{18}F-FDG μPET/CT image of a normal mouse and mice with 1 and 8 TPA challenges in the ears. Arrows: inflamed ears. The corresponding quantitative analysis of the FDG uptake in ears were shown. Data are expressed as mean ± SD (n=3/group). **p<0.01; ***p<0.001.

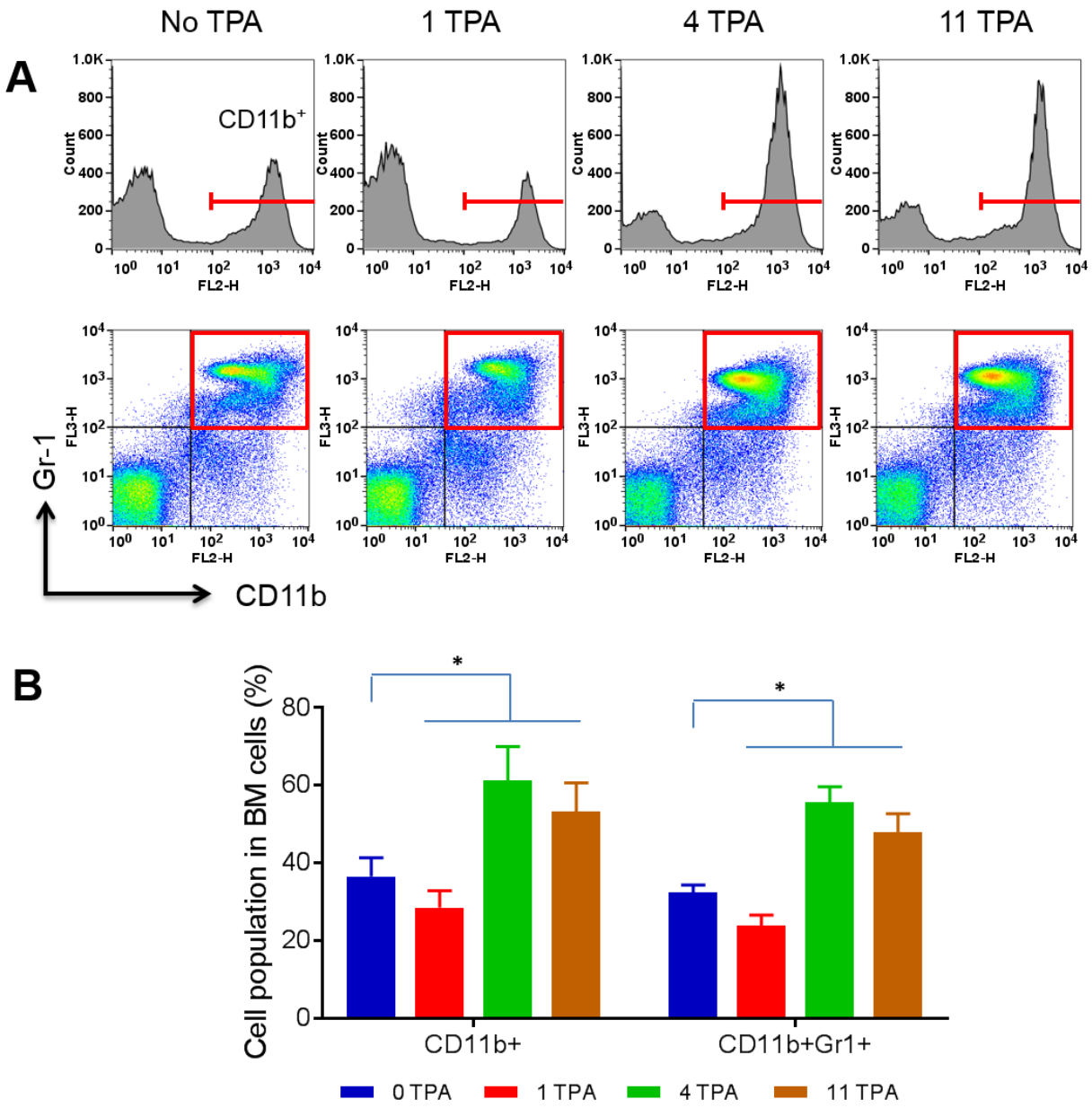

Figure 4. Flow cytometry analysis of bone marrow cells from mice with TPA-induced ear inflammation. (**A**) $CD11b^+$ cells and $CD11b^+Gr\text{-}1^+$ double-positive cells from bone marrow in mice with inflamed ears after 1, 4, and 11 TPA challenges. (**B**) Flow cytometric quantitation of the percentages of $CD11b^+$ cells and $CD11b^+Gr\text{-}1^+$ cells in whole bone marrow cells in normal mice (0 TPA) and mice with 1, 4, and 11 TPA challenges. BM, bone marrow. All data are expressed as mean ± SD (n=3/group). *$p<0.05$.

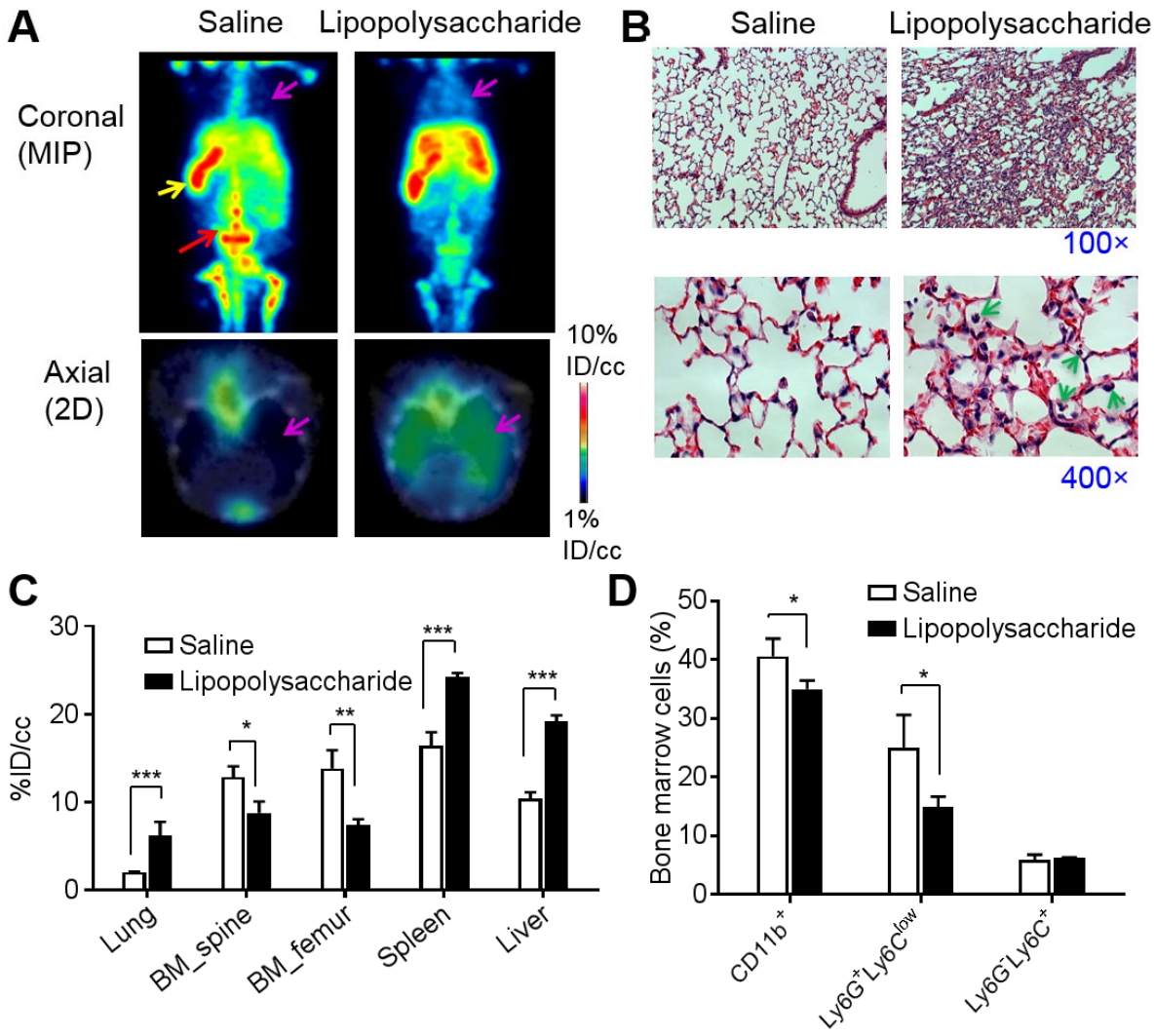

Figure 5. µPET/CT of ^{64}Cu-αCD11b in BALB/c mice with lipopolysaccharide-induced acute lung inflammation. (**A**) Representative µPET/CT images of a control mouse with intratracheal instillation of saline and a mouse with acute inflammation in the lung induced by intratracheal instillation of lipopolysaccharide. Images were acquired 24 h after intravenous injection of ^{64}Cu-αCD11b and 28 h after lipopolysaccharide instillation. Purple arrow: inflamed lung; red arrows: bone marrow; yellow arrows: spleen. MIP (maximum intensity projections); 2D (two-dimensional). (**B**) Representative H&E-stained lung tissues. Green arrows: granular leukocytes. (**C**) PET imaging quantification of ^{64}Cu-αCD11b in normal mice and mice with lung inflammation at 24 h. (**D**) Flow cytometry analysis of bone marrow cells from normal mice and mice with acute lung inflammation performed at 24 h. Data are expressed as mean ± SD (n=3/group). *p<0.05; **p<0.01; ***p<0.001.

Table of Contents

20 %ID/g) to highlight uptake of the radiotracer in the spleen.

Supplemental Figure 9. The representative flow cytometric dot plots showing bone marrow cells from normal mice and mice with acute lung inflammation.

MATERIALS AND METHODS

Number of DOTA per αCD11b Antibody

The average number of DOTA chelators per αCD11b antibody was measured according to reported procedure (*1-3*). Briefly, nonradioactive $CuCl_2$ (80-fold excess of DOTA-αCD11b) in 20 μL 0.1N sodium acetate (NaOAc) buffer (pH 5.5) was added to approximately 1.0 mCi $^{64}CuCl_2$ in 50 μL 0.1N NaOAc buffer, then, 20 μg of DOTA-αCD11b in 40 μL 0.1N NaOAc buffer were added to the above carrier-added $^{64}CuCl_2$ solution. The reaction mixture was incubated with constant shaking at 40°C for 1 h. The ^{64}Cu-DOTA-αCD11b (^{64}Cu-αCD11b) was purified by PD-10 column with 1 × PBS, and eluent (3.0–4.5 ml) was collected. The number of DOTA per αCD11b antibody was calculated using the following equation: number of DOTA per αCD11b antibody = moles (Cu^{2+}) × activity (3.0–4.5 mL)/moles (DOTA-αCD11b)/total activity (loaded for each labeling). The activities in the equation were all decay-corrected to the same time point. The results were expressed as mean ± SD (n = 3).

microPET Imaging Quantification

For each microPET scan, three-dimensional regions of interest (ROIs) were drawn over the major organs or inflammatory lesions on decay-corrected whole-body coronal images. The average radioactivity concentration (accumulation) with an organ or an inflammation lesion was obtained from mean pixel values within the ROI volume, and then converted to percentage injected dose per gram of tissue (%ID/g) or percentage injected dose per cubic centimeter of tissue (%ID/cc). Imaging data acquired from the Inveon scanner (Siemens) were analyzed using Inveon software (Siemens) and expressed as percentage injected dose per gram of tissue (%ID/g). Imaging data acquired from the Albira scanner (Bruker) were analyzed using PMOD software (PMOD Technologies, Ltd., Zurich, Switzerland) and expressed as percentage injected

dose per cubic centimeter of tissue (%ID/cc).

Competitive Cell-binding Assay

Freshly isolated BM cells from C57BL/6 mice were suspended in PBS containing 0.5% bovine serum albumin (1×10^5 cells per 200 μL). Cells were incubated with ^{64}Cu-αCD11b (0.1 μCi/well, ~$4x10^{-10}$ M) in the absence and presence of increasing concentration of nonradioactive αCD11b at room temperature for 2 h with gentle shaking. After removal of culture medium under vacuum, cells were washed 3 times with PBS containing 0.1% bovine serum albumin. Radioactivity of the cells from each well was counted with a gamma counter. The 50% inhibitory concentration of nonradioactive αCD11b was calculated by fitting the data with nonlinear regression using GraphPad Prism (GraphPad Software, La Jolla, CA).

Supplemental Table 1. Number of DOTA per αCD11b antibody on DOTA-αCD11b conjugate

DOTA/ αCD11b ratio	50:1
Number of DOTA per αCD11b	5.77 ± 0.394

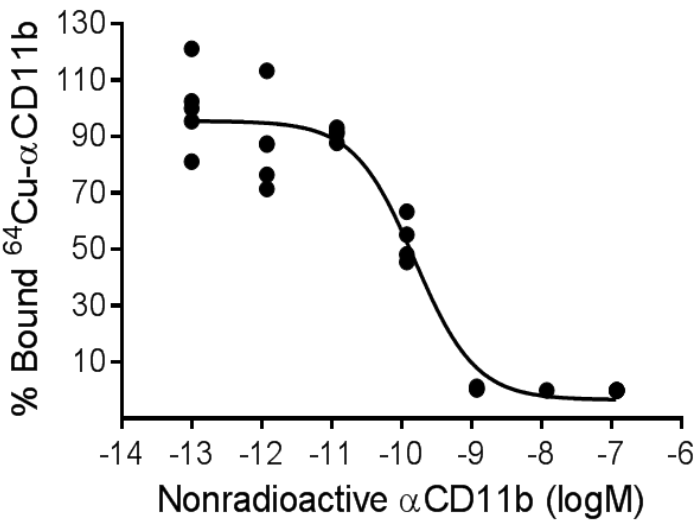

Supplemental Figure 1. Cell binding assay. Displacement of the binding of ^{64}Cu-αCD11b to bone marrow cells by nonradioactive αCD11b (n=5).

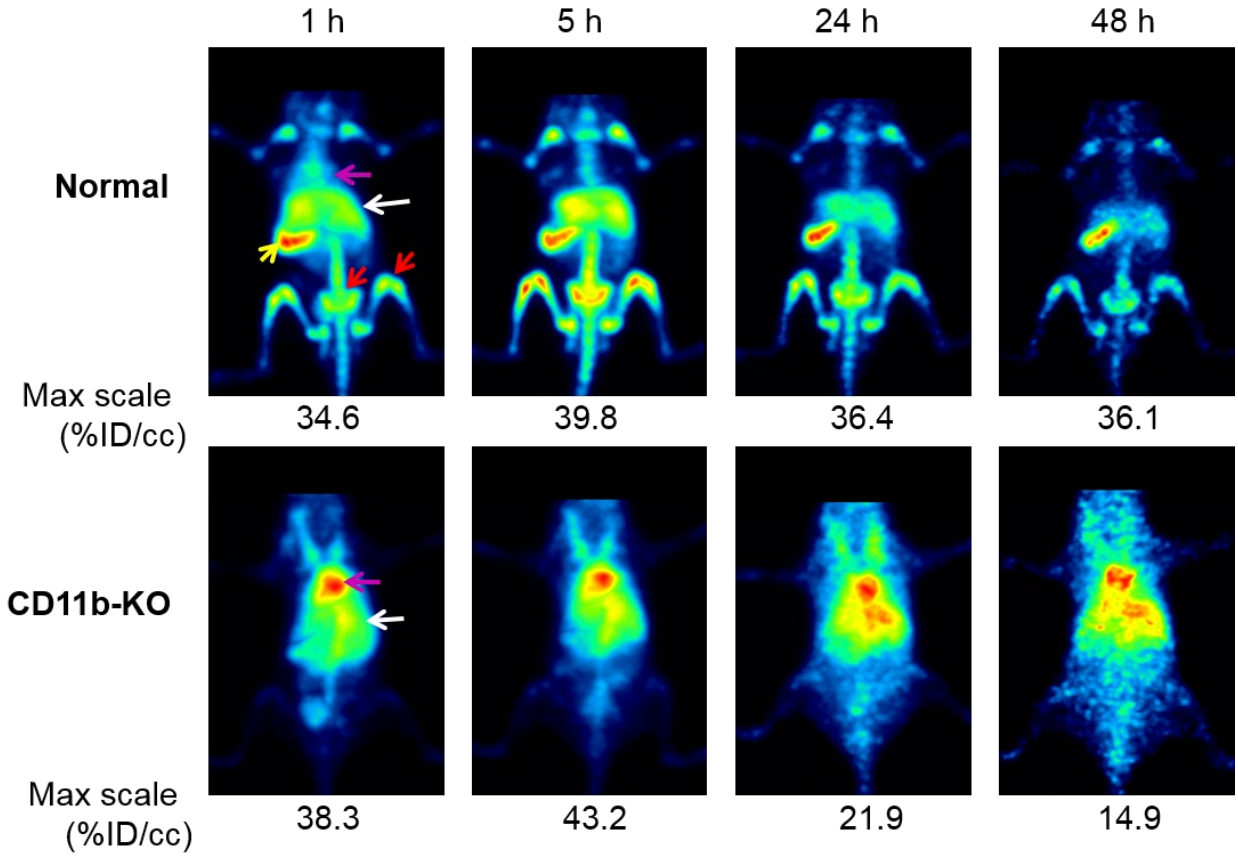

Supplemental Figure 2. Representative 3D maximum intensity projection (MIP) µPET images with ^{64}Cu-αCD11b on normal and CD11b knockout (CD11b-KO) C57BL/6 mice.

Red arrows: bone marrow; yellow arrows: spleen; white arrows: liver; purple arrows: heart (n=3).

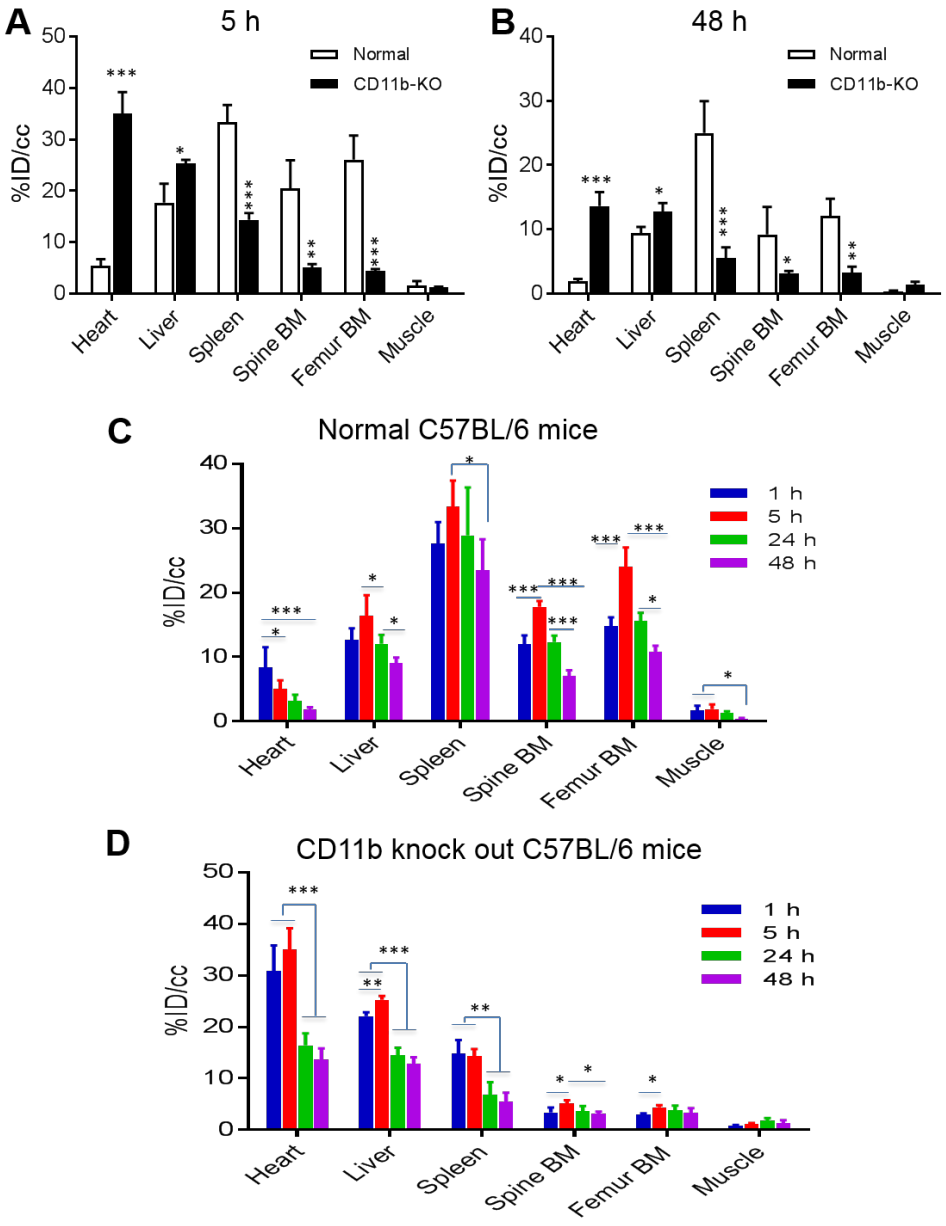

Supplemental Figure 3. Quantitative analysis of µPET/CT imaging data of ^{64}Cu-αCD11b in normal and CD11b-KO C57BL/6 mice. (**A, B**) Quantity analysis µPET/CT imaging data acquired at 5 h (**A**) or 48 h (**B**) after intravenous injection of ^{64}Cu-αCD11b. (**C, D**) Quantity µPET/CT imaging data in normal C57BL/6 mice (**C**) and CD11b-KO C57BL/6 mice (**D**) at 1, 5, 24, and 48 h after radiotracer injection. Data are expressed as mean ± SD (n=3/group).

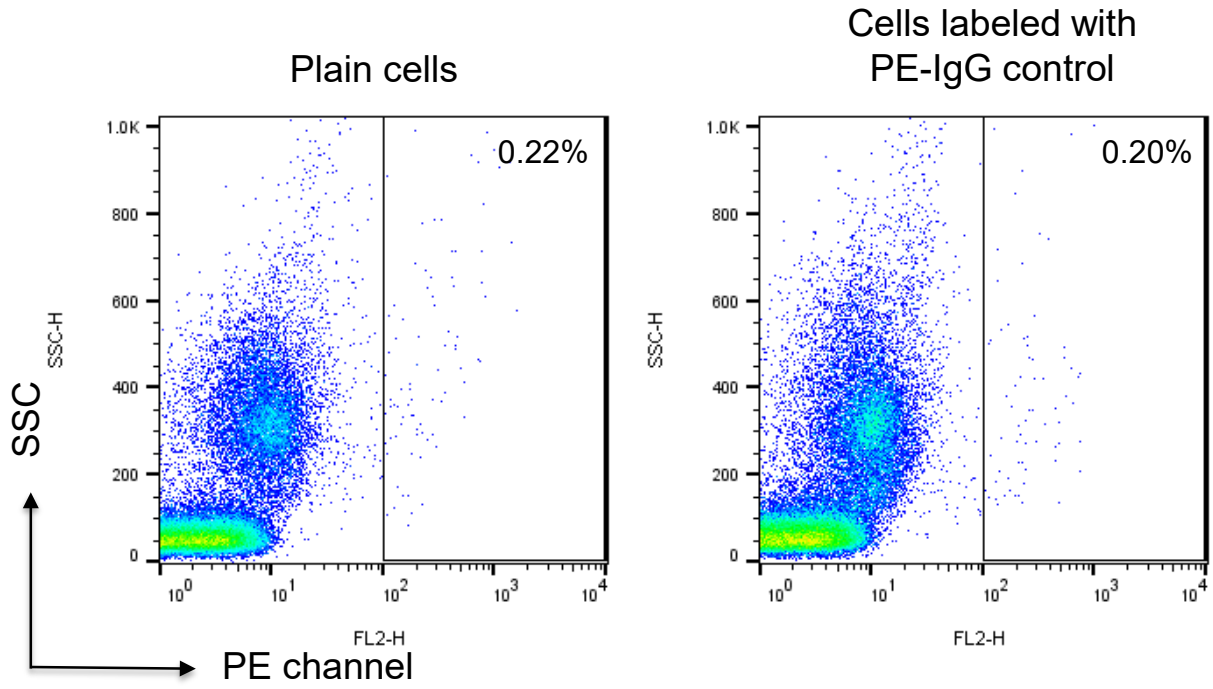

Supplemental Figure 4. Dot plot diagram of flow cytometry showing background signals from the PE channel for plain bone marrow cells and bone marrow cells treated with PE-IgG control.

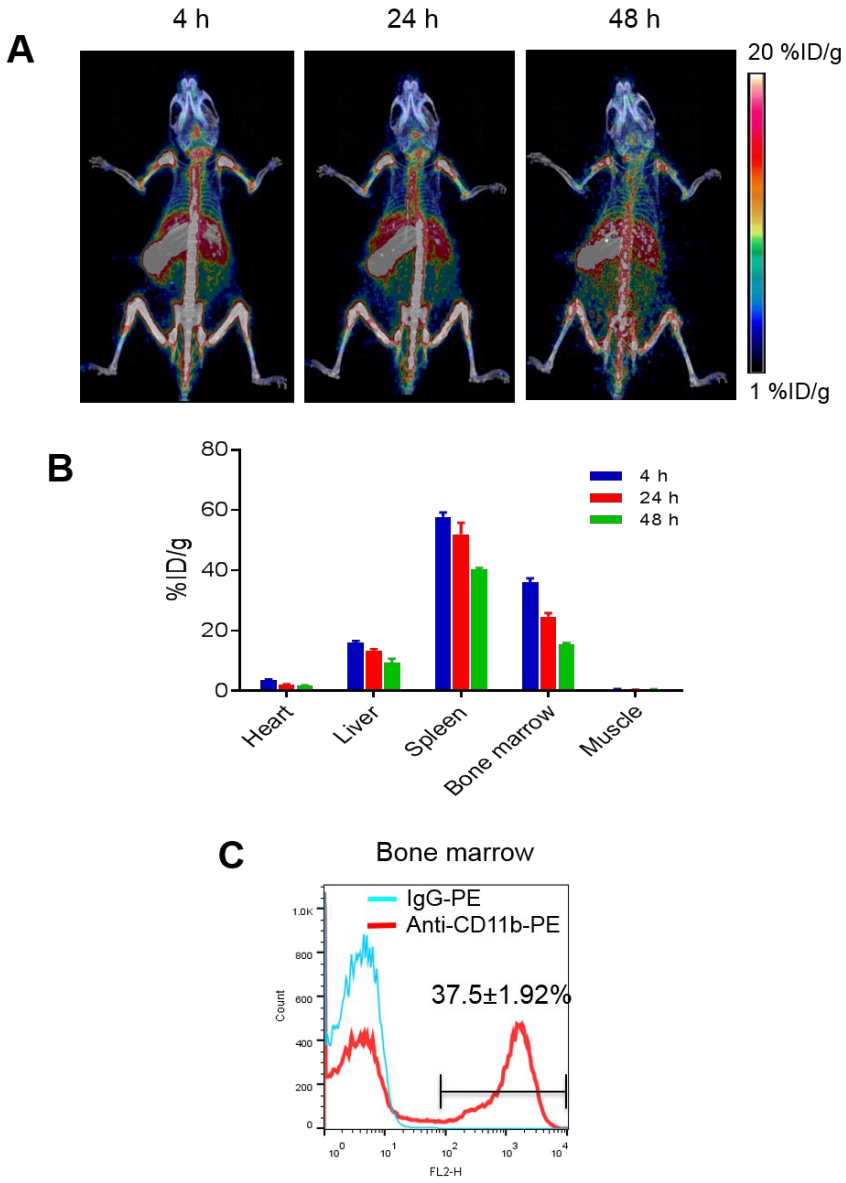

Supplemental Figure 5. ^{64}Cu-αCD11b μPET/CT in normal BALB/c mice. (**A**) Representative μPET/CT images of normal BALB/c mice at 4, 24, and 48 h after intravenous injection of ^{64}Cu-αCD11b. (**B**) Quantitative analysis of μPET/CT data showing distribution of ^{64}Cu-αCD11b in major organs at different times after radiotracer injection. (**C**) Flow cytometry analysis of CD11b^{+} myeloid cells in bone marrow. The resting bone marrow contains a large number of CD11b^{+} myeloid cells in BALB /c mice. Data were expressed as mean ± SD (n=3).

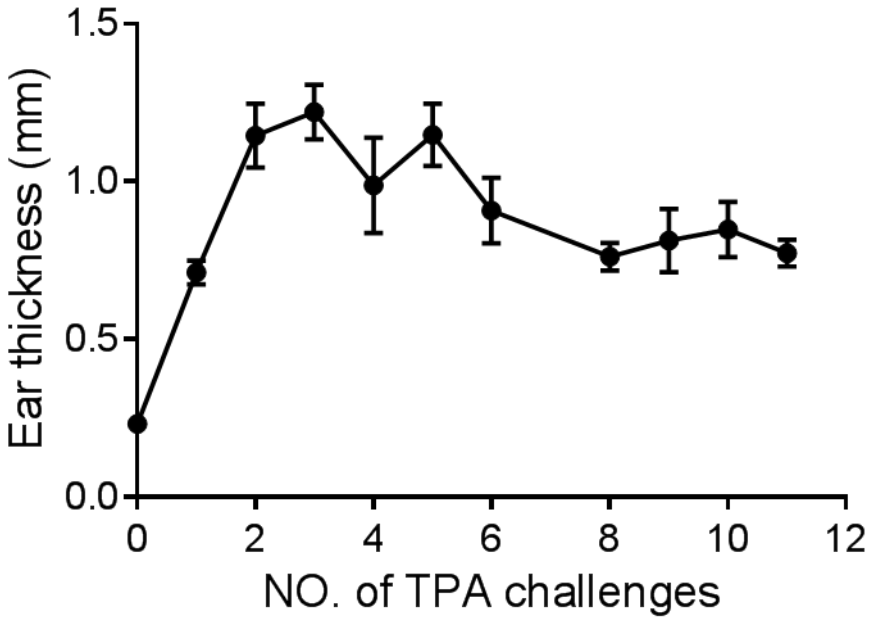

Supplemental Figure 6. Ear thickness after different numbers of TPA challenges on ear of BALB/c mice. Data are expressed as mean ± SD (n=8).

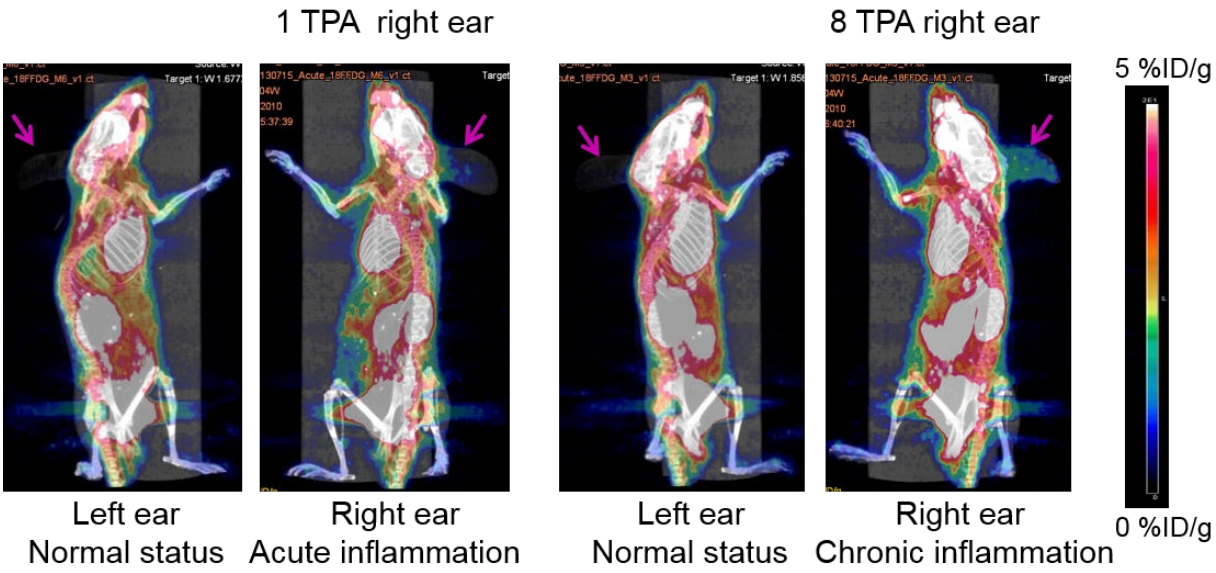

Supplemental Figure 7. 18F-FDG µPET/CT in BALB/c mice with TPA-induced acute and chronic ear inflammation. Images were presented at a color scale (0 – 5 %ID/g) different from that in Figure 3C (3 – 10 %ID/g) to highlight uptake of the radiotracer in the inflammation ear. Purple arrow: ear.

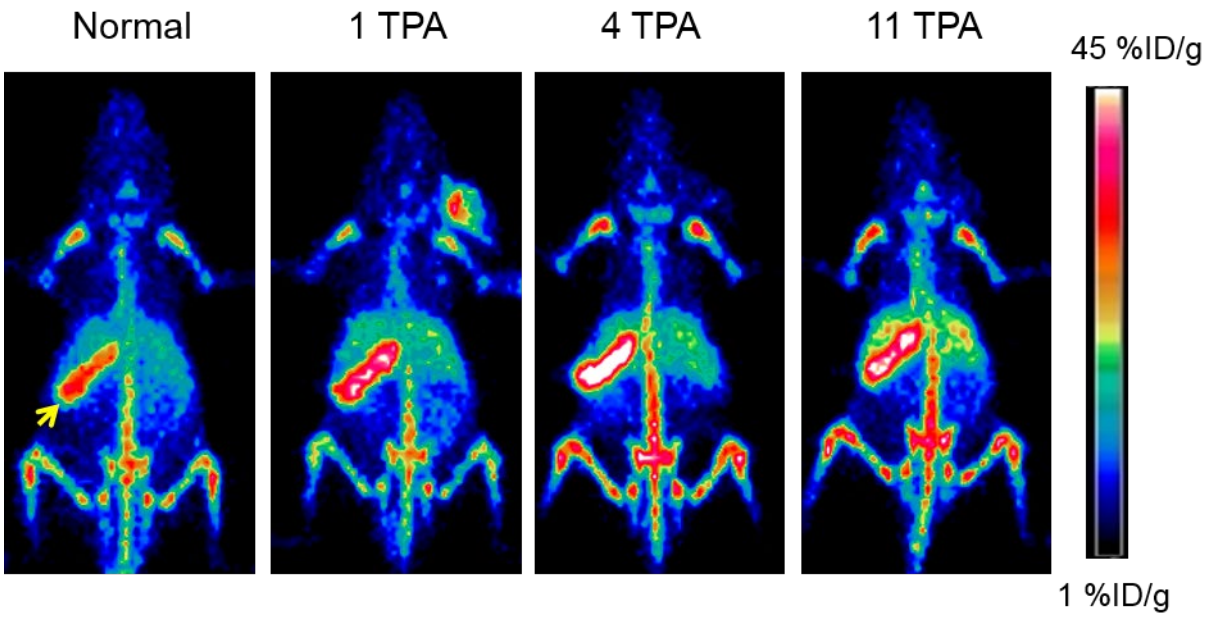

Supplemental Figure 8. ^{64}Cu-αCD11b μPET/CT in BALB/c mice with TPA-induced acute and chronic ear inflammation. Images were presented at a color scale (1 – 45 %ID/g) different from that in Figure 2 (1 – 20 %ID/g) to highlight changes in the spleen after different numbers of TPA challenges. Yellow arrow: spleen.

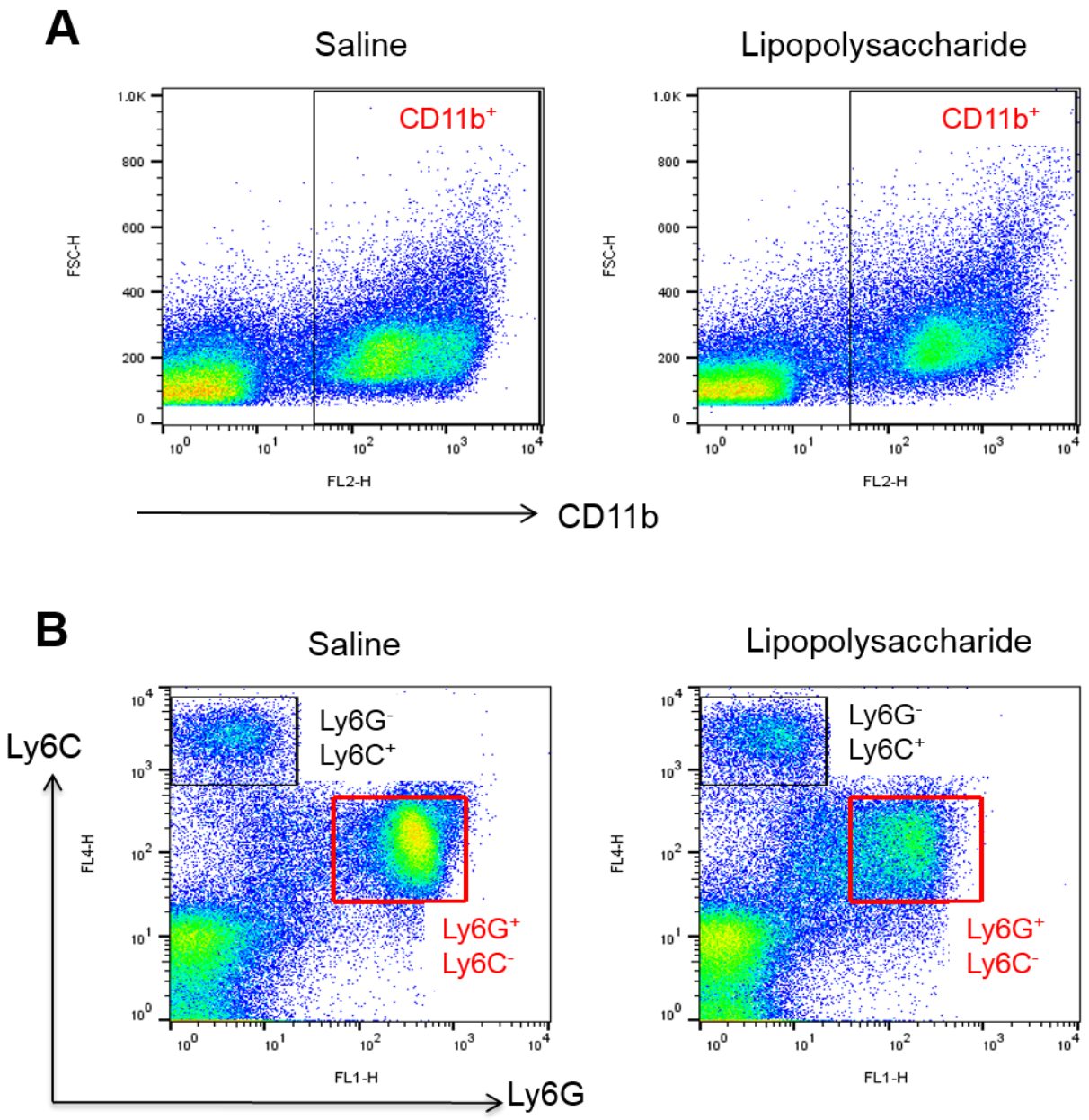

Supplemental Figure 9. The representative flow cytometric dot plots showing bone marrow cells from normal mice and mice with acute lung inflammation. Bone marrow cell samples were analyzed 24 h after tntratracheal instillation of lipopolysaccharide. (**A**) Black grid: $CD11b^+$ cells. (**B**) Black grid: $Ly6G^-Ly6C^+$ monocytic cells; red grid: $Ly6G^+Ly6C^{low}$ granulocytic cells.

REFERENCES

1. Cai W, Wu Y, Chen K, Cao Q, Tice DA, Chen X. In vitro and in vivo characterization of 64Cu-labeled Abegrin, a humanized monoclonal antibody against integrin alpha v beta 3. *Cancer Res.* 2006;66:9673-9681.

2. Meares CF, McCall MJ, Reardan DT, Goodwin DA, Diamanti CI, McTigue M. Conjugation of antibodies with bifunctional chelating agents: isothiocyanate and bromoacetamide reagents, methods of analysis, and subsequent addition of metal ions. *Anal Biochem.* 1984;142:68-78.

3. Liu S, Li D, Park R, et al. PET imaging of colorectal and breast cancer by targeting EphB4 receptor with 64Cu-labeled hAb47 and hAb131 antibodies. *J Nucl Med.* 2013;54:1094-1100.

The Journal of NUCLEAR MEDICINE

μPET/CT imaging of local and systemic immune response using ^{64}Cu-αCD11b

Qizhen Cao, Qian Huang, Chandra Mohan and Chun Li

J Nucl Med.
Published online: February 22, 2019.
Doi: 10.2967/jnumed.118.220350

The Journal of Nuclear Medicine is published monthly.
SNMMI | Society of Nuclear Medicine and Molecular Imaging
1850 Samuel Morse Drive, Reston, VA 20190.
(Print ISSN: 0161-5505, Online ISSN: 2159-662X)

SNMMI SOCIETY OF NUCLEAR MEDICINE AND MOLECULAR IMAGING